BG

LBL-36795
UC-413
Preprint

Lawrence Berkeley Laboratory
UNIVERSITY OF CALIFORNIA

Submitted to Nuclear Instruments and Methods
in Physics Research B

α-Particle Induced High-Energy γ-Ray Yields from Light Elements

R.K. Heaton, H.W. Lee, B.C. Robertson,
E.B. Norman, K.T. Lesko, and B. Sur

January 1995

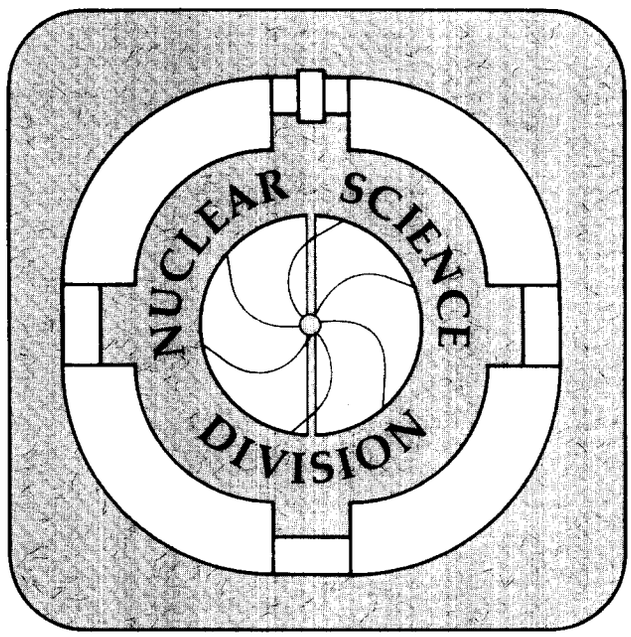

Prepared for the U.S. Department of Energy under Contract Number DE-AC03-76SF00098

LBL-36795
UC-413

α-Particle Induced High-Energy γ-Ray Yields from Light Elements

R.K. Heaton, H.W. Lee, and B.C. Robertson

Department of Physics
Queen's University
Kingston, Ontario, Canada

E.B. Norman, K.T. Lesko, and B. Sur

Nuclear Science Division
Lawrence Berkeley Laboratory
University of California
Berkeley, California 94720

January 1995

This work was supported by the the Natural Sciences and Engineering Research Council of Canada (NSERC), and by the Director, Office of Energy Research, Office of High Energy and Nuclear Physics, Division of High Energy Physics, of the U.S. Department of Energy under Contract No. DE-AC03-76SF00098.

α-Particle Induced High-Energy γ-Ray Yields from Light Elements [1]

R.K. Heaton, H.W. Lee, B.C. Robertson

Department of Physics, Queen's University

and

E.B. Norman, K.T. Lesko, B. Sur [2]

Lawrence Berkeley Laboratory

Abstract

Alpha-induced thick-target γ-ray yields from light elements have been measured in the energy range between 5.6 MeV $\leq E_\alpha \leq$ 10 MeV. The γ-ray yields above 2 MeV from thick targets of beryllium, boron nitride, sodium fluoride, magnesium, and aluminum were measured, and the results of this experiment were used to construct tables suitable for calculating the α-induced direct production γ-ray intensity distributions from materials. These results show a significant reduction compared with previous estimates of the distribution.

1 Introduction

In recent years there has been a growing interest in experiments to test the predictions of grand unified theories and extensions of electro-weak theories. These experiments, including proton decay, double beta decay and neutrino astrophysics investigations, typically involve measurements with low event rates and therefore require large detector volumes. In many cases events in these detectors can be mimicked or overwhelmed by background effects, in particular by high energy γ-rays. A significant number of γ-rays originate from natural radioactivity in the detector components and surrounding materials. Elements

[1] This work supported partly by a grant from NSERC and partly by the U.S. Department of Energy under contract #DE-AC03-76SF00098

[2] Present address: AECL Research, Chalk River Nuclear Laboratories, Chalk River, Canada K0J 1J0

of both the ^{238}U and ^{232}Th decay chains emit energetic α-particles which can react with light elements to produce these high energy γ-ray backgrounds.

The naturally occuring elements of the uranium and thorium decay chains produce γ-rays by several different mechanisms. Generally the largest source of high-energy γ-rays (E_γ >5 MeV) results from the capture of neutrons produced through both spontaneous fission and through the (α, n) reaction on light elements. Such a γ-ray source has been investigated and characterized by many researchers [1–6]. The spontaneous fission of uranium also produces some high energy γ-rays, but at a rate which can be neglected in most circumstances [7,3].

Since an understanding of the different α-induced γ-ray background components is crucial for the effective design and operation of low background experiments, several groups have presented detailed studies of this γ-ray source. In particular, Pomansky [3] has presented theoretical results indicating that $(\alpha, p\gamma)$ and $(\alpha, n\gamma)$ reactions produce substantially more high energy γ-rays than previously thought. This secondary γ-ray background source had not been considered significant and had not been investigated in other background studies. This background source, referred to here as the "direct production" source, is the focus of the present work.

The experimental setup is described in section 2 and the techniques used for analysis of the data is described in section 3. A summary of γ-ray yield measurements for Be, B, F, Na, Mg and Aℓ is provided in a form suitable for spectrum calculations in section 4. The results are discussed in section 5, and their use is illustrated by a calculation of this background for granite, a common environmental material. In addition, the significance of this background in situations where the neutron induced component is suppressed is illustrated through a consideration of α-induced direct production γ-ray background from photomultiplier tubes to be used in the Sudbury Neutrino Observatory.

2 The Experiment

Measurements of high energy γ-ray yields were performed using the facilities at the Lawrence Berkeley Laboratory's 88″ cyclotron. Since the primary purpose of this study was to determine the thick-target γ-ray yield, self-supporting thick targets of Be, BN, NaF, Mg and Aℓ were used in these measurements. Each target was sufficiently thick to completely stop the highest energy α-particle. Alpha beam energies of 10.0, 8.8, 7.7, 7.0, 6.3 and 5.6 MeV were used. The physical arrangement of the counting area is illustrated in figure 1.

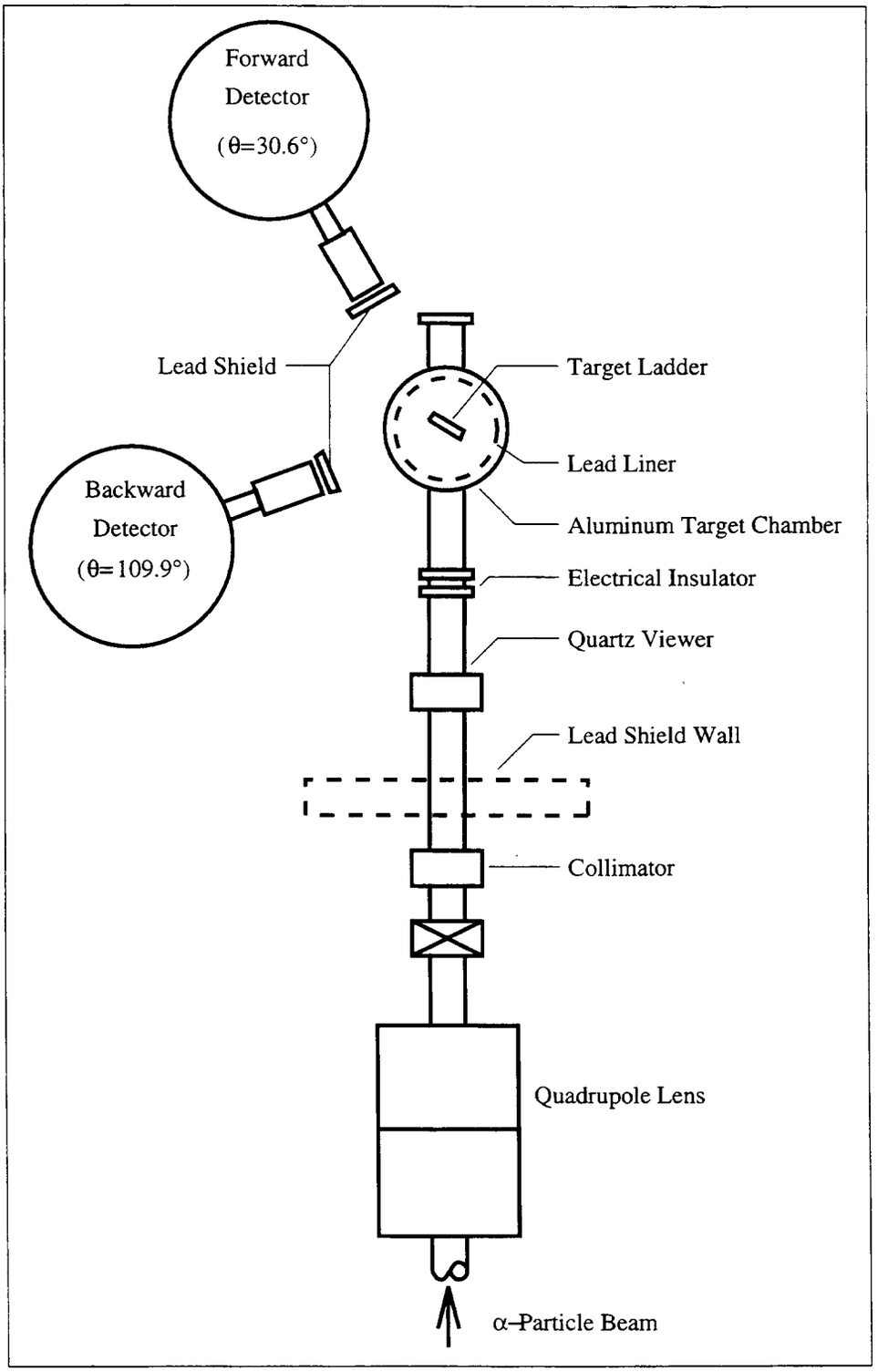

Fig. 1. The experiment target and counting area for the γ-ray measurements.

The emitted γ-rays were detected in two HPGe detectors, denoted as the forward and backward detectors, and located at 30.6° and 109.9° with respect to the incident beam direction and approximately 19 cm and 15 cm from the target, respectively. The low energy γ-ray counting rate was reduced by placing a 0.95 cm thick lead shield directly in front of each detector. The signals from the forward detector were processed by an Ortec 572 amplifier, while the backward detector used a Canberra 2021 amplifier. In the initial 10 MeV runs, the unipolar output of each amplifier was input directly into an Ortec PC/MCA system. In subsequent runs, a low energy cutoff of approximately 2 MeV was implement by triggering an Ortec 442 linear gate and stretcher with an Ortec 551 timing SCA. The SCA generated a gating pulse whenever the bipolar amplifier signal exceeded an adjustable lower energy threshold. On receiving a gating signal, the linear gate and stretcher passed the delayed unipolar amplifier signal through to the MCA.

The targets were attached to an aluminum target ladder with 2.22 cm diameter target holes. A 0.16 cm thick lead shield with corresponding 1.91 cm diameter holes shielded the aluminum holder from the α-particle beam. The target ladder was rotated 30° clockwise from the beam direction to minimize the interference of the target ladder shield with γ-rays produced in the target. The current on target was measured by a beam current integrator which generated one count for each nC of charge on target. Beam current leakage and secondary electron effects were minimized by collecting the beam current from the combined target ladder and target chamber. The target chamber was electrically isolated from the rest of the beam line as shown in figure 1. Beam currents were adjusted to maintain the detector dead times to between 15 and 25%, as reported by the MCA units. All targets except for Be were exposed to currents ranging from 4 to 100 nA, while the more active Be target was exposed to currents typically between 1 and 20 nA. Beam position and diameter were monitored using a quartz phosphor on the target ladder which could be viewed remotely through a camera. The beam spot diameter was between 0.3 cm and 0.6 cm.

Pile-up and dead time were monitored by placing a pulser signal on the test input of each detector preamp. The pulse generators were externally triggered by the beam current integrator. The pulser voltage was adjusted to place the pulser peak in the high energy (> 10 MeV) region of each spectrum, except during the 10 MeV runs in the forward angle detector when it was placed in the low energy portion of the spectrum.

3 Analysis

In order to determine the total absolute γ-ray yield for each transition, the area of each peak in a spectrum was extracted, and the residual nucleus transition identified. Some of the most significant identified transitions from Aℓ are indicated in figure 2, which shows the high-energy portion of the E_α = 10 MeV spectrum. The peaks in the spectrum are identified by both the reaction and transition. Only escape peaks used in the yield calculations are labelled, and can be distinguished from full energy peaks by a trailing (1^{st}) and (2^{nd}) label for a first and second escape peak, respectively. At 7620 keV, a low-level contamination arising from neutron capture on iron can also be seen.

Each peak area was converted into an absolute yield using the integrated beam current, the pulser-measured live time, and the measured detector efficiencies. The measured transition yields from reactions with a particular target nucleus were then combined into 1 MeV wide bins to permit convenient spectrum calculations such as those presented here. The yields from individual transitions is reported elsewhere [16].

3.1 Peak Areas

The α-particle kinematics coupled with the use of thick targets in this experiment and the energy dependence of the excitation cross section resulted in a complex shape for the γ-ray peaks which could not be parameterized reliably. Therefore, the area of each peak was determined from the difference between the total number of counts in the peak region and the interpolated background area beneath it.

The background for each peak was defined by three regions: one on either side of the peak, plus a region underlying the peak. The side regions were chosen to be as close to the peak as possible, while still free of significant interference from either the principal or neighbouring peaks. The underlying background was defined as either linear or quadratic in shape, with an optional step at the centroid position. All parameters except the centroid were calculated using a weighted least squares fit. After the background parameters had been calculated, the centroid of the peak was recalculated, and the fit parameters were adjusted to reflect a shift of the fit origin. In instances where a step background was used, the dependence of the centroid calculation on the position of the step necessitated the iteration of the centroid calculation until the centroid position converged on a stationary value.

The least squares fitting of the background function used weights based on the

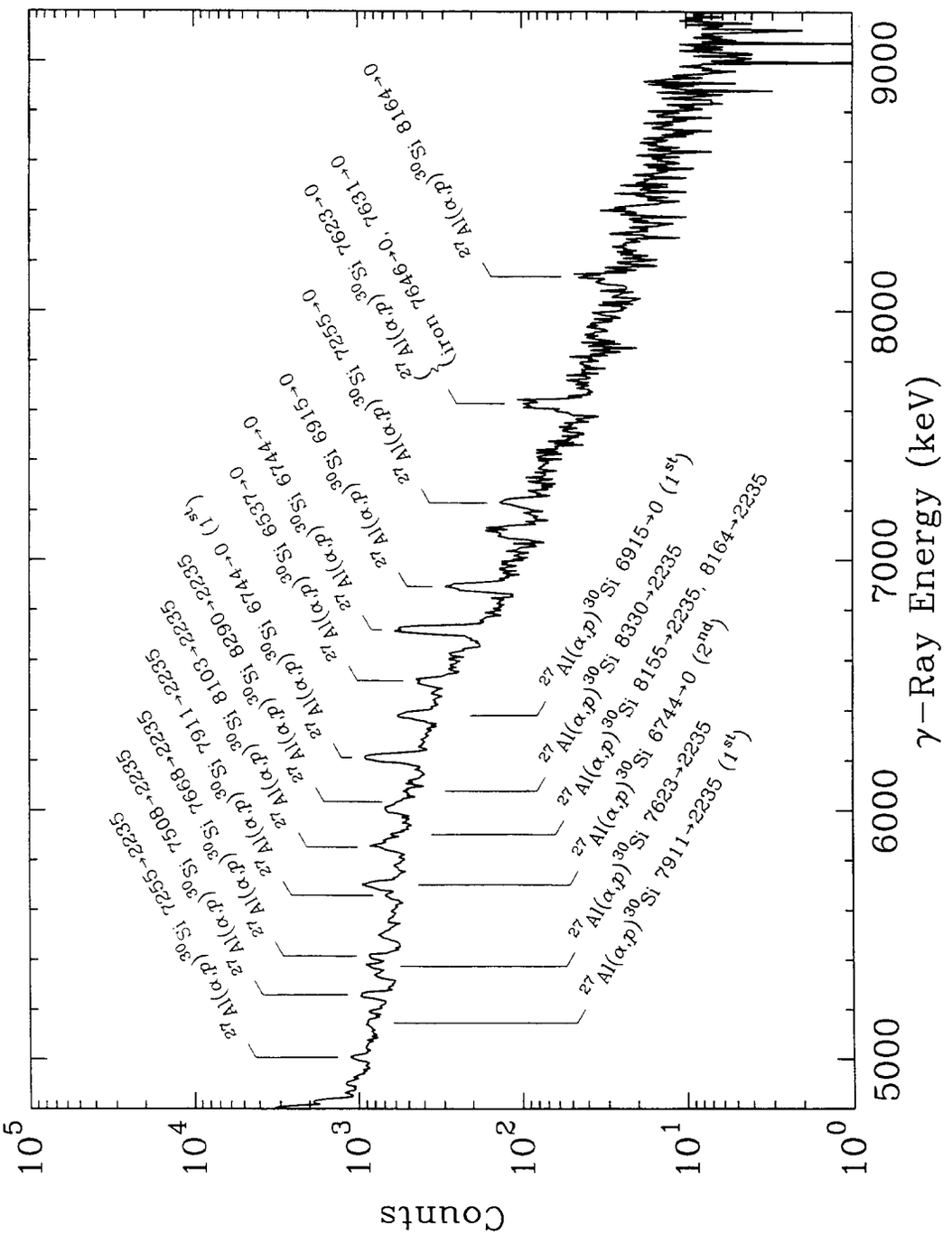

Fig. 2. A portion of the high energy γ-ray spectrum from Aℓ for 10 MeV α-particles is shown for the backward angle detector. The major transitions used in the yield calculations have been identified. Several unidentified peaks represent escape peaks which were subtracted from the spectrum during analysis.

fitted parent distribution. Since the weights were then a function of the fitting parameters themselves, the fitting process was iterated until the fit parameters converged. This procedure avoided the underestimate of the background region area that typically results from using statistical weights.

In a number of cases, adjacent peaks were not fully separated and contained a significant contribution from nearby peaks. In these cases, the peak areas were separated by fitting each peak to a Gaussian shape. The background was first calculated as described previously, with a peak region encompassing the combined peaks. This background was then subtracted from the spectrum in the peak region, and the resulting spectrum was fit to a two-Gaussian function by a non-linear least-squares calculation. The area of each peak was taken as the total number of counts in the doublet peak region weighted by the fractional area of each Gaussian.

In some instances, escape peaks from higher energy transitions interfered with background and area calculations of full energy peaks of lower energy transitions. This interference was removed by subtracting the escape contribution using the measured full energy peak intensity and the known detector response. The response was determined as described below.

3.2 Detector Efficiency Characterization

The absolute full energy peak efficiency of each detector was determined using a combination of calibrated sources, uncalibrated sources and Monte Carlo calculations. A series of Monte Carlo calculations was used to determine a functional form for the detector peak efficiencies between 0.5 and 10 MeV. These efficiencies also supplemented the high energy efficiency data where few γ-ray source measurements were available.

A total of five calibrated standard sources were used to characterize the detector system: ^{60}Co, ^{137}Cs, ^{56}Mn, ^{22}Na and ^{238}Pu–^{13}C. The first four sources were used to calibrate a ^{56}Co source, which provided absolute efficiency measurements up to 3.6 MeV. A measurement at 6.13 MeV was provided by a ^{238}Pu–^{13}C source. The Monte Carlo characterization of the experimental detector system was used to constrain the efficiency above 4 MeV according to the known γ-ray interaction cross sections.

The absolute detector efficiency was found to be accurately parameterized between the energy range from 0.5 and 10 MeV by an equation of the form

$$e_{\text{eff}}(E) = \frac{\exp\left[f(E)\right]}{1 + \exp\left[\frac{E-a_0}{a_1}\right]} \tag{1}$$

where $f(E)$ is a second order polynomial in γ-ray energy E, and the a_i are constants. The coefficients for this equation were obtained from a least squares fit to the source measurement data and normalized Monte Carlo results. The normalization of the Monte Carlo results was obtained using source data above 2 MeV, since uncertainties in modelling detector dead regions caused difficulties in matching the efficiency maximum near 600 keV. The sensitivity of the normalization to the 2 MeV cut was estimated by varying the cut between 1.5 MeV and 3 MeV. The normalization varied by approximately 5% for this range of cuts, and showed deviations of up to 15% from the measured 6.13 MeV calibration value. Based on this, an uncertainty of 15% was attributed to the normalization, and was applied to the Monte Carlo data used in the calibration.

The measured relative escape peak efficiencies were in agreement with those determined by the Monte Carlo simulation. Both calibrated and uncalibrated sources were used to measure the ratio of the escape peak to the full energy peak areas. The use of area ratios eliminated the dependence of these efficiencies on the source strength, and also allowed the use of some of the data from the target runs. This additional data significantly increased the number of data points available above 4 MeV. The relative escape peak properties were taken from the Monte Carlo calculations and normalized to the experimental data. The averaged experimental data for the single escape efficiency was found to be $100.3 \pm 1.0\%$ and $100.4 \pm 0.8\%$ of the Monte Carlo results, while for the double escape efficiency was found to be $97.1 \pm 1.0\%$ and $98.4 \pm 1.0\%$ of the Monte Carlo results for the forward and backward detectors respectively.

3.3 Yield Determinations

The γ-ray yield calculation for a given transition incorporated three distinct steps. The peak areas were determined as discussed above. Second, the net peak areas were converted into γ-ray yields for each detector. Finally, the individual detector yields were used to determine the total isotropic yield for each transitions.

The conversion from peak areas to absolute γ-ray yields was achieved by dividing the peak area by the detector efficiency at the peak centroid energy, the number of α-particles on target, and by the dead time and pile-up corrections. The number of α-particles on target was recorded by the scaler counter, and the dead time and pile-up corrections were monitored by the counts placed in the pulser peak of each spectra.

The angular γ-ray yield measurements were fit to a Legendre polynomial expansion, from which the P_0 coefficient provided the γ-ray yield into 4π. The

analysis assumed that the counts for each peak in each detector could be expressed solely in terms of the P_0 and P_2 components of the Legendre polynomial expansion of the γ-ray angular distribution. The detector positions were chosen near the zeros of the P_4 component of the Legendre polynomial in order to minimize the contribution of higher order terms in the expansion. A small correction for the finite detector geometry was made by approximating the contribution of each Legendre polynomial to the detector yield by the integral of the polynomial intensity over the area of each detector face.

Each of the absolute detection efficiency, detector live time, and α-particle count on target contributed to the systematic uncertainty of the measured yield. The detector efficiency contributed a γ-ray energy dependent uncertainty between 1% and 10%, in addition to a 3.5% uncertainty reflecting the measured sensitivity to target positioning and reproducibility of efficiency measurements. The live time in each detector was determined for runs other than $E_\alpha = 10$ MeV to within 1% from the area of the pulser peak inserted into each spectrum; in some cases this uncertainty was increased in the forward detector by gain instabilities, and in the backward detector by a pile-up of γ-ray counts on the tail of the pulser peak. In no case did the live time uncertainty exceed 6%. In the 10 MeV runs, the live time was deduced from the counting rate in each detector due to a failure of the live time monitor system. This determination introduced an additional uncertainty of less than 10% in the detector live time, except for the Aℓ and Be targets, where an uncertainty of close to 20% was assessed for the forward detector.

The total number of particles on target was determined by the number of counts generated by the beam current integrator and accumulated in the scaler. The pulser system was triggered by the same signal as the current scaler, so that the area of the pulser peak determined the live-time corrected particles on target. In this way, the beam count uncertainty was included in the determination of the live time uncertainty. The only additional uncertainty assigned to the number of particles on target was in the $E_\alpha = 8.8$ MeV runs, where beam source focusing difficulties lead to a significant target beam spot halo. This resulted in a $23 \pm 10\%$ loss of particles onto the target ladder lead shielding as determined from a comparison of specific transition yields with measurements reported by other groups. A comparison of our yields with the cross sections of Seamster *et al* [8] for the 2230 keV and 2210 keV γ-rays from the ^{27}Aℓ+α and the ^{24}Mg(α, p) reactions respectively is shown in figure 3. All our yields for these γ-rays are in agreement within our adopted uncertainty and the estimated 10% uncertainty of the cross section measurements.

The yield measurements for beryllium are also consistent with the cross sections reported by other researchers. These yields are approximately 15% lower than those calculated using the cross sections of Geiger and van der Zwan [9,10], who measured the cross section for the associated neutron group with an

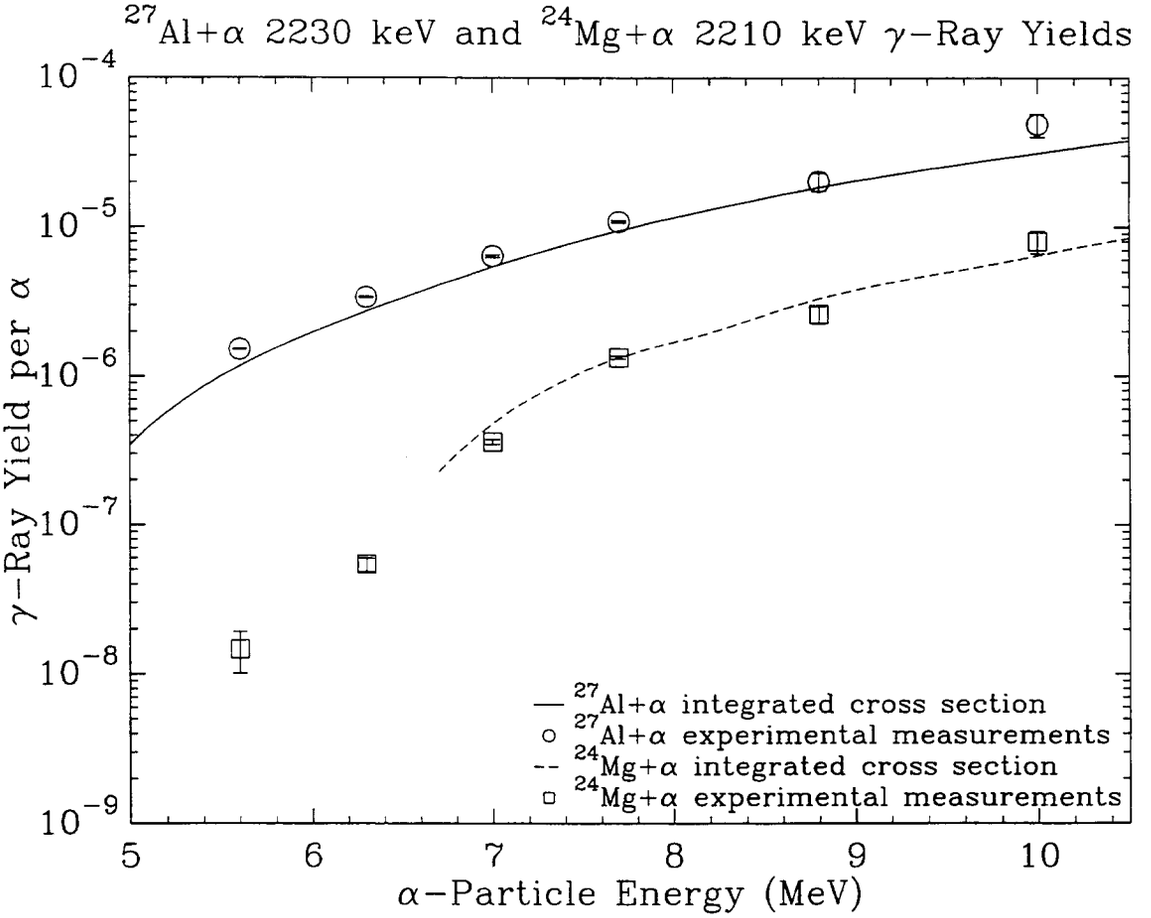

Fig. 3. The 2230 keV and 2210 keV γ-ray yield from the Aℓ and Mg targets, respectively. The points indicate the yield measurements, while the lines indicate the thick-target yield calculated from an integration of the cross sections, measured in 0.1 to 0.5 keV intervals, of Seamster *et al.* The Aℓ target data sets contain the yield from the 2230 keV and 2210 keV γ-rays resulting from the (α, p) and (α, α') reactions respectively.

uncertainty between 11 and 16%. The relative measurements of the differential γ-ray cross section by Seaborn *et al* [11] were used to extend this comparison above 8 MeV by scaling to the total cross sections of Geiger and van der Zwan in the region of overlap. These cross sections agreed to within 30% with four cross section measurements in the same energy range by Verbinski *et al* [12], who estimated a 10% systematic uncertainty in their measurements. Our yield measurements at the two highest α-particle energies are consistent with the cross section derived yields within this uncertainty and fall 10% higher than the derived yields at 8.8 and 10 MeV.

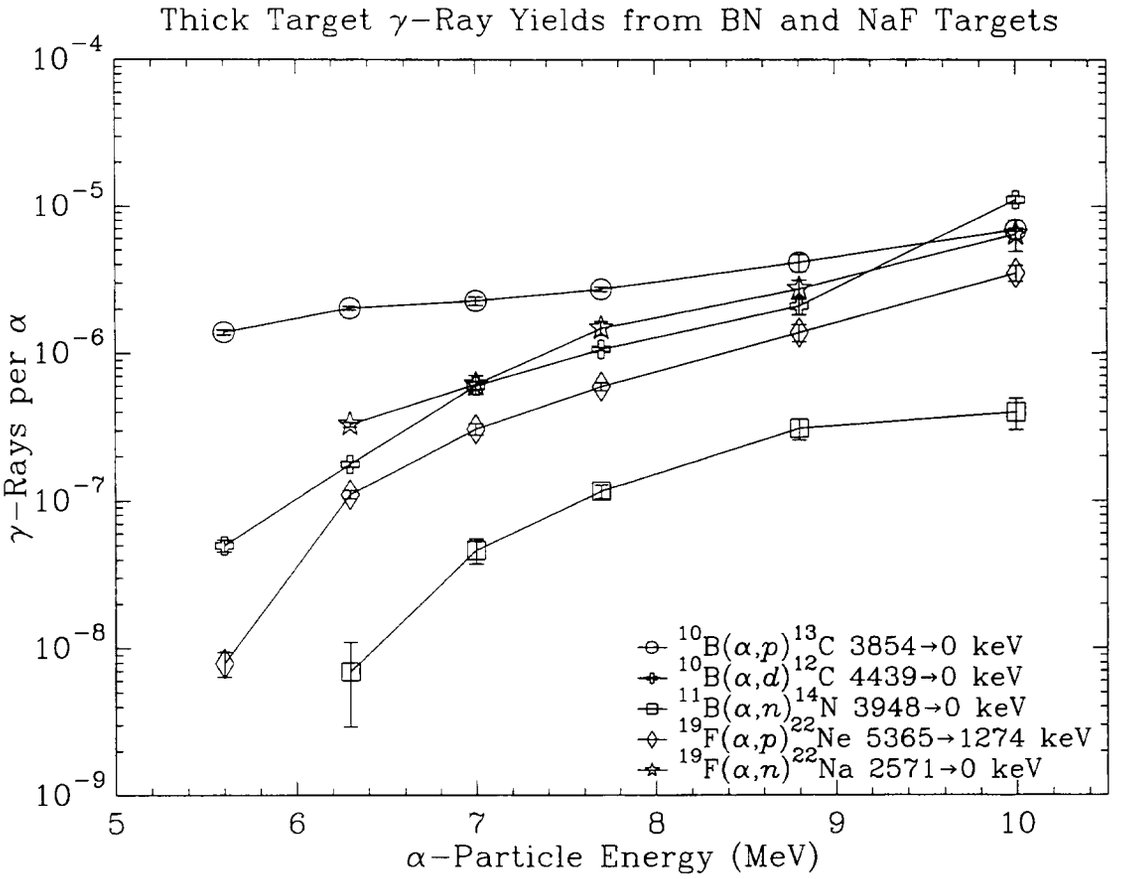

Fig. 4. Selected yields from the BN and NaF targets. Only yields from peaks with unique identifications have been shown. The joining line between yields is provided as a visual aid only.

4 Results

The yields were calculated from the combined full energy and escape peak yields when available. The escape and full energy peak yields were found to be in agreement within statistical uncertainties in all cases. A representative sample of the thick-target γ-ray yields is shown in figures 4 and 5. These yields correspond to single transition peaks from various reactions, and have been adjusted to reflect the yield from elemental targets. The thick-target yields in most cases are a smooth function of energy. The yields for individual transitions change by as much as three orders of magnitude between 5.6 and 10 MeV α-particle energies. All thick-target yields follow the expected monotonic decrease with α-particle energy. In some instances, such as the $^{10}\mathrm{B}(\alpha,d)^{12}\mathrm{C}$ 4439 $\rightarrow$ 0 keV reaction in figure 4 and the $^{24}\mathrm{Mg}(\alpha,p)^{27}\mathrm{A}\ell$ 3004 $\rightarrow$ 0 keV reaction of figure 5, the effects of strong resonances cause a significant change in the yield behaviour.

In the highest α-particle energy runs, the most significant source of uncer-

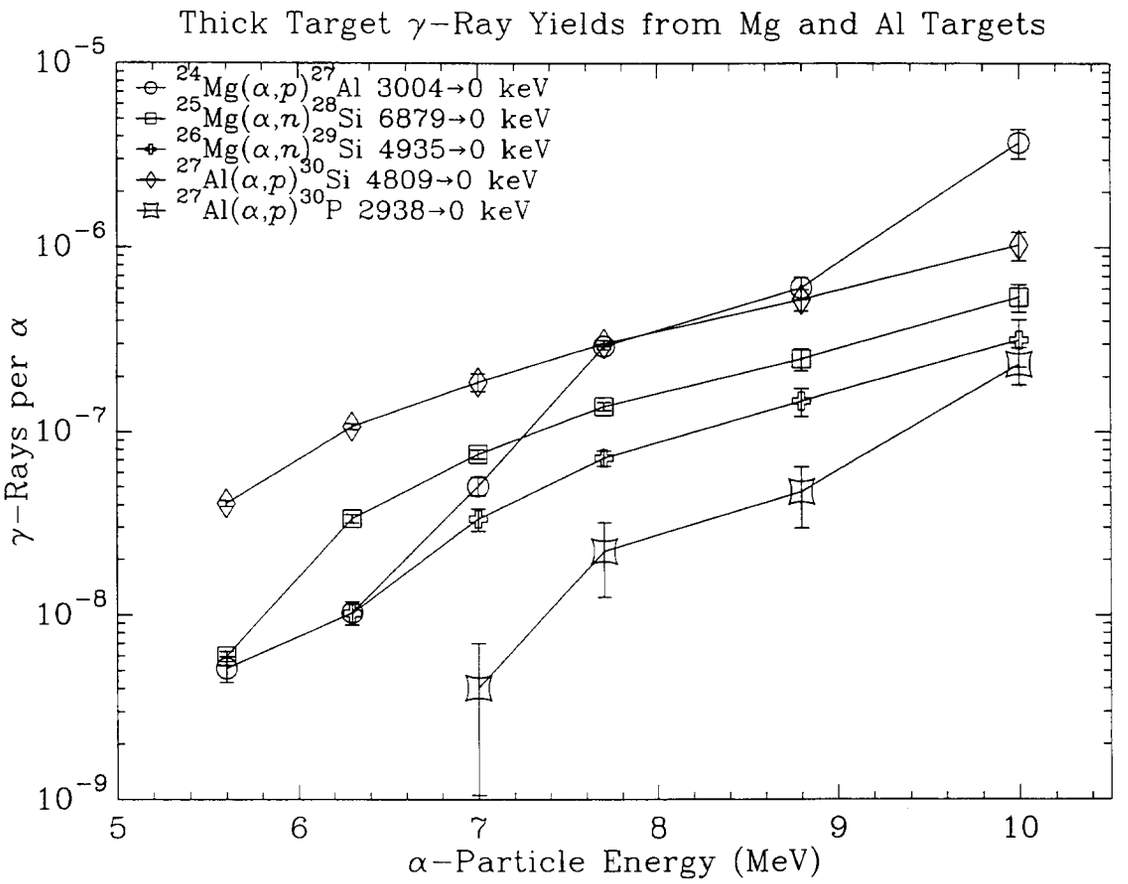

Fig. 5. Selected yields from the Mg and Aℓ targets. Only the thick-target yields from peaks with unique identifications have been shown. The line joining measure yields is provided as a visual aid only.

tainty resulted from the 10 MeV live time determinations and the 8.8 MeV beam halo adjustment. The 10 MeV live time determination introduced uncertainties ranging from as much as 15% for the Aℓ and Be targets to as little as 3% in the NaF target. At other energies, the detector live time typically contributed between 0.5% and 2% to the yield uncertainty. The detector efficiency uncertainties, discussed previously, played a more significant role with contributions as large as 11%. Statistical uncertainties in the peak area accounted for a contribution on the order of 10% to 15% for all but the weakest transitions. Uncertainties based on the selection of the background shape were typically of the same order as the statistical uncertainties, with values ranging from 2% to 15% in most cases. In cases where branching ratios were required to separate individual transitions, the branching uncertainty typically added between 10% and 25% to the total uncertainty in the yield. Branching ratios were primarily used in the calculation of the NaF target yields.

Only yields from the NaF target were significantly affected by ambiguous γ-ray transition identifications. In cases where a spectrum peak was associated

with reactions from both target nuclei, published decay schemes were used to separate the yields where possible. In cases where only an estimate of a transition yield from a minor contributor to the total peak was available, a 100% uncertainty for that contributor was adopted. In most cases these estimated yields only accounted for a small fraction of the yield attributed to a given energy bin. An exception to this is found between 2 and 3 MeV, where a large peak associated with both the ^{23}Na$(\alpha,n)^{26}$Aℓ 2069 $\rightarrow$ 0 keV and the ^{19}F$(\alpha,p)^{22}$Ne 3357 $\rightarrow$ 1274 keV yield accounts for about 70% of the yield from the target in this energy range. In this case, the yield was divided equally between the two reactions with a 100% uncertainty adopted for both yields. This uncertainty dominates the total uncertainty for this energy range in both the fluorine and sodium yields.

Our experimental results are summarized in tables 1 through 7. The tables consist of the thick-target γ-ray yields for each element, summed into 1 MeV wide bins. These elements consist of common light elements with favourable Q-values for the production of high energy γ-rays. All α-particle energies investigated, except for 10 MeV, correspond to the range of primary α-particle energies encountered in the natural uranium and thorium decay chains. The 10 MeV measurement provided a limiting measurement for the highest possible yield. The yield for each element has been adjusted to correspond to elementally pure targets with normal isotopic abundances. The yields measured from the composite BN and NaF targets were adjusted according to the ratio of the stopping powers of the individual elements in each target [4]. For example in the BN target, this resulted in a multiplication of the observed boron yields by a factor of 2.30. Similarly, for the NaF target, the fluorine yields were multiplied by 2.25 and the sodium yields by 1.80. Variations of 0.5% in the calculated stopping power ratios were obtained over the beam energies considered here; this uncertainty has been neglected in these yield tables.

The uncertainties quoted in these tables contain both the statistical and systematic uncertainties discussed previously. The statistical uncertainties from individual transitions were summed in quadrature, while the separate systematic uncertainties were simply added, and the total uncertainty in each bin determined from a quadrature sum of the individual statistical and systematic uncertainties for the bin. The summation of a number of individual transitions within each bin is responsible for the dominance of the systematic component of the yield uncertainty. In this presentation of our data, no attempt has been made to separate γ-rays of a similar energy resulting from different reactions on the same element in the target.

In the measurement of the boron γ-ray yield, the ^{11}B$(\alpha,n)^{14}$N 2313 keV transition was contaminated by inelastic scattering of α-particles on ^{14}N. This contamination was removed by subtracting the (α,α') contribution using an inte-

Table 1
4439 keV γ-Ray Yield in Beryllium (γ-ray quanta MeV^{-1} per α)

γ-Ray energy Range (MeV)	α-Particle Energy (MeV)					
	10 MeV	8.8 MeV	7.7 MeV	7.0 MeV	6.3 MeV	5.6 MeV
4 – 5	$(1.18 \pm 0.23) \cdot 10^{-4}$	$(1.03 \pm 0.14) \cdot 10^{-4}$	$(7.06 \pm 0.31) \cdot 10^{-5}$	$(6.38 \pm 0.25) \cdot 10^{-5}$	$(5.66 \pm 0.25) \cdot 10^{-5}$	$(4.06 \pm 0.16) \cdot 10^{-5}$

Table 2
Binned γ-Ray Yield in Boron† (γ-ray quanta MeV^{-1} per α)

γ-Ray Energy Range (MeV)	α-Particle Energy (MeV)					
	10 MeV	8.8 MeV	7.7 MeV	7.0 MeV	6.3 MeV	5.6 MeV
2 – 3	$(5.17 \pm 0.23) \cdot 10^{-5}$	$(1.20 \pm 0.26) \cdot 10^{-5}$	$(8.49 \pm 0.35) \cdot 10^{-6}$	$(4.53 \pm 0.33) \cdot 10^{-6}$	$(1.96 \pm 0.08) \cdot 10^{-6}$	$(8.62 \pm 0.45) \cdot 10^{-7}$
3 – 4	$(1.37 \pm 0.06) \cdot 10^{-5}$	$(6.66 \pm 0.91) \cdot 10^{-6}$	$(4.08 \pm 0.17) \cdot 10^{-6}$	$(3.39 \pm 0.25) \cdot 10^{-6}$	$(2.99 \pm 0.76) \cdot 10^{-6}$	$(2.13 \pm 0.11) \cdot 10^{-6}$
4 – 5	$(1.25 \pm 0.07) \cdot 10^{-5}$	$(2.40 \pm 0.33) \cdot 10^{-6}$	$(1.16 \pm 0.05) \cdot 10^{-6}$	$(6.00 \pm 0.44) \cdot 10^{-7}$	$(1.77 \pm 0.09) \cdot 10^{-7}$	$(4.97 \pm 0.50) \cdot 10^{-8}$
5 – 6	$(1.10 \pm 0.04) \cdot 10^{-5}$	$(9.78 \pm 1.32) \cdot 10^{-7}$	$(2.00 \pm 0.09) \cdot 10^{-7}$	—	—	—
6 – 7	$(7.43 \pm 0.49) \cdot 10^{-7}$	—	—	—	—	—

† See discussion of 17 MeV giant dipole resonance γ-ray

Table 3
Binned γ-Ray Yield in Nitrogen (γ-ray quanta MeV^{-1} per α)

γ-Ray Energy Range (MeV)	α-Particle Energy (MeV)		
	10 MeV	8.8 MeV	7.7 MeV
2 – 3	$(2.09 \pm 0.38) \cdot 10^{-6}$	$(5.23 \pm 1.02) \cdot 10^{-7}$	$(2.42 \pm 0.18) \cdot 10^{-7}$
3 – 4	$(4.71 \pm 0.22) \cdot 10^{-6}$	$(1.35 \pm 0.36) \cdot 10^{-7}$	—

Table 4
Binned γ-Ray Yield in Fluorine (γ-ray quanta MeV^{-1} per α)

γ-Ray Energy Range (MeV)	α-Particle Energy (MeV)					
	10 MeV	8.8 MeV	7.7 MeV	7.0 MeV	6.3 MeV	5.6 MeV
2 – 3	$(7.58 \pm 2.08) \cdot 10^{-5}$	$(1.93 \pm 0.72) \cdot 10^{-5}$	$(9.30 \pm 3.35) \cdot 10^{-6}$	$(3.04 \pm 2.18) \cdot 10^{-6}$	$(1.51 \pm 1.14) \cdot 10^{-6}$	$(9.15 \pm 0.44) \cdot 10^{-7}$
3 – 4	$(1.72 \pm 0.19) \cdot 10^{-5}$	$(5.63 \pm 0.58) \cdot 10^{-6}$	$(3.21 \pm 0.13) \cdot 10^{-6}$	$(2.09 \pm 0.18) \cdot 10^{-6}$	$(8.73 \pm 0.41) \cdot 10^{-7}$	$(2.77 \pm 0.13) \cdot 10^{-7}$
4 – 5	$(1.37 \pm 0.15) \cdot 10^{-5}$	$(3.42 \pm 0.49) \cdot 10^{-6}$	$(1.39 \pm 0.09) \cdot 10^{-6}$	$(6.17 \pm 0.64) \cdot 10^{-7}$	$(1.78 \pm 0.14) \cdot 10^{-7}$	$(1.99 \pm 0.31) \cdot 10^{-8}$
5 – 6	$(2.62 \pm 0.34) \cdot 10^{-6}$	$(7.38 \pm 1.12) \cdot 10^{-7}$	$(2.59 \pm 0.23) \cdot 10^{-7}$	$(9.24 \pm 1.01) \cdot 10^{-8}$	$(3.54 \pm 0.39) \cdot 10^{-8}$	$(8.50 \pm 1.75) \cdot 10^{-9}$
6 – 7	$(1.63 \pm 0.27) \cdot 10^{-6}$	$(9.33 \pm 2.01) \cdot 10^{-8}$	—	—	—	—
7 – 8	$(2.81 \pm 0.94) \cdot 10^{-7}$	—	—	—	—	—

Table 5
Binned γ-Ray Yield in Sodium (γ-ray quanta MeV^{-1} per α)

γ-Ray Energy Range (MeV)	α-Particle Energy (MeV)					
	10 MeV	8.8 MeV	7.7 MeV	7.0 MeV	6.3 MeV	5.6 MeV
2 – 3	$(3.56 \pm 1.61) \cdot 10^{-5}$	$(1.26 \pm 0.57) \cdot 10^{-5}$	$(6.41 \pm 2.67) \cdot 10^{-6}$	$(4.47 \pm 1.77) \cdot 10^{-6}$	$(2.19 \pm 0.92) \cdot 10^{-6}$	$(5.15 \pm 0.26) \cdot 10^{-7}$
3 – 4	$(8.13 \pm 1.25) \cdot 10^{-6}$	$(2.22 \pm 0.43) \cdot 10^{-6}$	$(9.35 \pm 1.63) \cdot 10^{-7}$	$(5.51 \pm 0.61) \cdot 10^{-7}$	$(1.32 \pm 0.09) \cdot 10^{-7}$	$(3.23 \pm 0.32) \cdot 10^{-8}$
4 – 5	$(2.16 \pm 0.80) \cdot 10^{-6}$	$(2.37 \pm 0.96) \cdot 10^{-7}$	$(1.16 \pm 0.26) \cdot 10^{-7}$	$(7.51 \pm 1.11) \cdot 10^{-8}$	$(3.51 \pm 0.77) \cdot 10^{-8}$	$(8.49 \pm 2.47) \cdot 10^{-9}$
5 – 6	$(4.43 \pm 1.50) \cdot 10^{-7}$	$(8.27 \pm 2.07) \cdot 10^{-8}$	—	—	—	—

Table 6
Binned γ-Ray Yield in Magnesium (γ-ray quanta MeV^{-1} per α)

γ-Ray Energy Range (MeV)	α-Particle Energy (MeV)					
	10 MeV	8.8 MeV	7.7 MeV	7.0 MeV	6.3 MeV	5.6 MeV
2 – 3	$(2.88 \pm 0.49) \cdot 10^{-5}$	$(1.00 \pm 0.13) \cdot 10^{-5}$	$(5.06 \pm 0.20) \cdot 10^{-6}$	$(2.41 \pm 0.15) \cdot 10^{-6}$	$(1.18 \pm 0.06) \cdot 10^{-6}$	$(4.89 \pm 0.28) \cdot 10^{-7}$
3 – 4	$(6.73 \pm 1.19) \cdot 10^{-6}$	$(1.30 \pm 0.19) \cdot 10^{-6}$	$(5.87 \pm 0.28) \cdot 10^{-7}$	$(1.47 \pm 0.12) \cdot 10^{-7}$	$(5.40 \pm 0.36) \cdot 10^{-8}$	$(2.13 \pm 0.16) \cdot 10^{-8}$
4 – 5	$(3.24 \pm 0.57) \cdot 10^{-6}$	$(9.01 \pm 1.29) \cdot 10^{-7}$	$(4.00 \pm 0.21) \cdot 10^{-7}$	$(2.39 \pm 0.18) \cdot 10^{-7}$	$(1.11 \pm 0.07) \cdot 10^{-7}$	$(2.97 \pm 0.18) \cdot 10^{-8}$
5 – 6	$(1.33 \pm 0.23) \cdot 10^{-6}$	$(5.52 \pm 0.76) \cdot 10^{-7}$	$(2.93 \pm 0.12) \cdot 10^{-7}$	$(1.76 \pm 0.13) \cdot 10^{-7}$	$(8.89 \pm 0.53) \cdot 10^{-8}$	$(1.55 \pm 0.11) \cdot 10^{-8}$
6 – 7	$(1.19 \pm 0.20) \cdot 10^{-6}$	$(3.91 \pm 0.57) \cdot 10^{-7}$	$(1.66 \pm 0.12) \cdot 10^{-7}$	$(9.02 \pm 0.67) \cdot 10^{-8}$	$(3.36 \pm 0.22) \cdot 10^{-8}$	$(5.97 \pm 0.42) \cdot 10^{-9}$
7 – 8	$(6.14 \pm 1.57) \cdot 10^{-7}$	$(2.22 \pm 0.36) \cdot 10^{-7}$	$(1.09 \pm 0.09) \cdot 10^{-7}$	$(5.65 \pm 0.58) \cdot 10^{-8}$	$(1.60 \pm 0.13) \cdot 10^{-8}$	—
8 – 9	$(1.03 \pm 0.27) \cdot 10^{-7}$	$(1.89 \pm 0.42) \cdot 10^{-8}$	$(5.45 \pm 1.74) \cdot 10^{-9}$	$(1.82 \pm 0.91) \cdot 10^{-9}$	—	—
9 – 10	$(7.16 \pm 1.72) \cdot 10^{-8}$	—	...	...	—	—

Table 7
Binned γ-Ray Yield in Aluminum (γ-ray quanta MeV^{-1} per α)

γ-Ray Energy Range (MeV)	α-Particle Energy (MeV)					
	10 MeV	8.8 MeV	7.7 MeV	7.0 MeV	6.3 MeV	5.6 MeV
2 – 3	$(7.07 \pm 1.24) \cdot 10^{-5}$	$(2.62 \pm 0.36) \cdot 10^{-5}$	$(1.42 \pm 0.08) \cdot 10^{-5}$	$(7.54 \pm 0.66) \cdot 10^{-6}$	$(3.78 \pm 0.19) \cdot 10^{-6}$	$(1.68 \pm 0.08) \cdot 10^{-6}$
3 – 4	$(2.14 \pm 0.39) \cdot 10^{-5}$	$(9.53 \pm 1.33) \cdot 10^{-6}$	$(5.02 \pm 0.28) \cdot 10^{-6}$	$(2.57 \pm 0.23) \cdot 10^{-6}$	$(1.30 \pm 0.07) \cdot 10^{-6}$	$(4.57 \pm 1.64) \cdot 10^{-7}$
4 – 5	$(3.32 \pm 0.56) \cdot 10^{-6}$	$(9.27 \pm 1.27) \cdot 10^{-7}$	$(4.62 \pm 0.27) \cdot 10^{-7}$	$(2.11 \pm 0.24) \cdot 10^{-7}$	$(1.09 \pm 0.06) \cdot 10^{-7}$	$(4.07 \pm 0.21) \cdot 10^{-8}$
5 – 6	$(7.45 \pm 1.36) \cdot 10^{-7}$	$(6.44 \pm 1.53) \cdot 10^{-8}$	$(7.74 \pm 2.32) \cdot 10^{-9}$	—		—
6 – 7	$(7.76 \pm 1.40) \cdot 10^{-7}$	$(2.18 \pm 0.30) \cdot 10^{-7}$	$(9.21 \pm 0.56) \cdot 10^{-8}$	$(1.77 \pm 0.18) \cdot 10^{-8}$	—	—
7 – 8	$(8.74 \pm 1.92) \cdot 10^{-8}$	$(1.53 \pm 0.31) \cdot 10^{-8}$	$(4.55 \pm 1.17) \cdot 10^{-9}$	—	—	—
8 – 9	$(2.99 \pm 0.72) \cdot 10^{-8}$	—	—	—	—	—

gration of the cross sections reported by Dyer *et al* [13]. These cross sections indicate an (α, α') thick-target elemental yield for this γ-ray of 3.01×10^{-6} at $E_\alpha = 10$ MeV, 9.12×10^{-7} at $E_\alpha = 8.8$ MeV, and 1.06×10^{-7} at $E_\alpha = 7.7$ MeV. A 10% uncertainty in these yields was adopted based on the uncertainty reported by Dyer *et al.* At 10 MeV, the (α, n) reaction accounted for less than 13% of the total yield, and at 7.7 MeV accounted for less than 3% of the yield.

The high energy γ-ray resulting from the giant dipole resonance in ^{10}B has not been included in these tables [14,15]. This 17 MeV γ-ray, which is above the energy range investigated in this study, has an unusually large cross section on the order of several microbarns below $E_\alpha = 10$ MeV [15]. Based on these cross sections, the estimated γ-ray yield from a boron target with normal isotopic abundance is 2.5×10^{-10} quanta per α at $E_\alpha = 8.8$ MeV, 1.2×10^{-10} quanta per α at 7.7 MeV, and 6.9×10^{-12} quanta per α at 7.0 MeV, with an estimated uncertainty of 15%. Although this γ-ray occurs with a comparatively weak yield, its high energy and consequent low attenuation suggests it should be considered and added to any backgrounds calculated from the yields listed in table 2.

5 Discussion

One of the primary aims of this study was to provide the information required to calculate the direct production α-induced γ-ray intensity distributions for materials containing trace concentrations of the uranium and thorium decay chains. Such spectra, together with other calculations of the spontaneous fission and radiative neutron capture contributions, enable a characterization the γ-ray background from the radioactive content of these materials. Both the uranium and thorium chains emit a number of α-particles with energies, listed in table 8, in the range covered by our measurements. These α-particle energies and intensities were used to calculate the γ-ray spectra from the ^{238}U and ^{232}Th chains in several materials. Since the uncertainties quoted in the yield tables are largely dominated by systematic uncertainties, our calculations using these tables have combined and propagated the uncertainties linearly, rather than in quadrature.

The γ-ray intensity distributions were calculated by summing the yields obtained for each α-particle energy, $Y_\alpha(E_\alpha)$, using a logarithmic interpolation for each energy range given by

$$\ln Y_\alpha(E_\alpha) = \ln Y_i + \frac{E_\alpha - E_i}{E_{i+1} - E_i} \ln\left(\frac{Y_{i+1}}{Y_i}\right) \qquad (2)$$

Table 8
Equilibrium α-Particle Intensity from the ^{238}U and ^{232}Th Decay Chains

^{238}U			^{232}Th		
α-Emitter	Average α-Particle Energy (MeV)	α-Particle Intensity per decay ^{238}U	α-Emitter	Average α-Particle Energy (MeV)	α-Particle Intensity per decay ^{232}Th
^{238}U	4.19	1.0	^{232}Th	4.00	1.0
^{234}U	4.76	1.0	^{228}Th	5.40	1.0
^{230}Th	4.66	1.0	^{224}Ra	5.65	1.0
^{226}Ra	4.77	1.0	^{220}Rn	6.29	1.0
^{222}Rn	5.49	1.0	^{216}Po	6.78	1.0
^{218}Po	6.00	1.0	^{212}Bi	6.05	0.36
^{214}Po	7.69	1.0	^{212}Po	8.78	0.64
^{210}Po	5.31	1.0			

where the i and $i+1$ subscripts indicate the tabulated yields Y at energies E bracketing the α-particle energy, E_α, for each element in the material. This logarithmic interpolation scheme is based on the observed exponential dependence of the thick-target yield on α-particle energy. In instances where the lower energy yield was zero, a linear interpolation was used. A number of the α-particles in both chains have energies below the lowest energy measurement at 5.6 MeV in this study. The contribution of these α-particles to the γ-ray spectrum was obtained through an extrapolation using equation (2) with data from the two lowest measured α-particle energies. The contribution of each elemental yield to the spectrum was obtained through a stopping power-weighted sum of the individual yields [4] using the stopping power of Ziegler [20].

For most elements, yield contributions due to α-particles with energies below our lowest measured energy were small. The contribution from α-particles with energies less than 5.6 MeV was largest for the lightest elements, and more important for the uranium chain due to a greater number of α-particles emitted with energies around 4 MeV. The extrapolated yields contributed less than 10% to γ-ray yields above 5 MeV for each element in both the uranium and thorium chains. Below this γ-ray energy, the yields for Be from the uranium chain were most sensitive to the extrapolation, with as much of 60% of the uranium chain yield and 20% of the thorium chain yield coming from α-particles with energies less than 5.6 MeV. A comparison of this yield calculation to a calculation supplemented by Be yields between $E_\alpha = 4$ and 5.6 MeV derived from the cross sections of Geiger and van der Zwan [9,10]

Table 9
Composition of Materials for γ-Ray Spectrum Calculations

Element	Material Composition by Mass	
	Granite	Photomultiplier Tube Glass
B	—	7.00%
O	44.32%	53.50%
Na	2.86%	3.20%
Mg	0.67%	—
Al	9.09%	2.10%
Si	30.08%	30.70%
K	4.69%	2.80%
Ca	2.59%	—
Mn	0.25%	—
Fe	5.40%	—

agreed within 10% for the uranium chain, and within 4% for the thorium chain. The B yields below $E_\gamma = 4$ MeV contained up to a 50% contribution for the uranium chain and 20% for the thorium chain from α-particles below 5.6 MeV. The γ-ray yields for F below $E_\gamma = 3$ MeV also contained a contribution from low energy α-particles, with 25% and 6% of the uranium and thorium yield, respectively, attributed to α-particles with energies less than 5.6 MeV. All other targets at low γ-ray energies contained no more than a 20% yield contribution in the uranium chain and 5% in the thorium chain at γ-ray energies above 2 MeV. this extrapolation had no effect on yields above $E_\gamma =$ 4 MeV except for Be. In most applications, γ-rays from the (α, p) and (α, n) reactions below 4 MeV are a minor component of the total γ-ray spectrum, and so uncertainties introduced by this extrapolation can be largely ignored.

The calculated γ-ray intensity distribution for granite, a common host rock for several low-background laboratories, with a composition given in table 9 is shown in figure 6 for a thorium mass fraction which is five times that of the uranium mass fraction. The theoretical intensity distribution of Pomansky [3] for the direct production of γ-rays through the $(\alpha, n\gamma)$ and $(\alpha, p\gamma)$ reactions in granite is also shown in this figure. Our experimental yield falls considerably below that reported by Pomansky using the calculations of Glotov [3,22,23]. This difference appears to arise from their use of experimental $^{25}\mathrm{Mg}(\alpha, n)$ yield measurements for the calculation of the $^{27}\mathrm{A}\ell(\alpha, p)$ yield. In many rocks, including granite, the high-energy γ-ray intensity is dominated by the contribution from aluminum. The ^{25}Mg neutron yield was used as an estimate of the

total $^{27}\mathrm{A}\ell(\alpha,p)$ yield, based on the similarity of the reaction Q-values and the charge independence of nuclear forces. Although Pomansky and Glotov took the proton Coulomb barrier penetration effects into account in calculating the resulting excitation of the residual nucleus, our measurements indicate that the high-energy γ-ray production rate from ^{25}Mg is approximately an order of magnitude larger than that for aluminum, and so could account for the observed discrepancy.

The intensity distribution in figure 6 labelled "present results" was derived from the measured Na, Mg and Aℓ elemental γ-ray yields. These elements constituted 13% by weight of the granite and were exceeded in composition only by oxygen and silicon. Only the rare ^{17}O and ^{18}O oxygen isotopes have a favourable Q-value for producing γ-rays, and only through the (α,n) reaction. The total neutron yield from the (α,n) reaction in oxygen for α-particles up to 10 MeV has been reported, and is known to be a factor of 50 smaller than the total neutron yield from aluminum [4]. Since more than half the aluminum γ-rays come from the (α,p) reaction, it is expected that the elemental γ-ray yield from oxygen would be only 1% that of aluminum, and therefore contribute no more than 5% to the granite γ-ray intensity distribution. The inelastic scattering of α-particle off ^{16}O may contribute to the high energy γ-ray yield at high α-particle energies through excitation of the 6.13 MeV level. An integration using cross sections from an exponential extrapolation from the 10 MeV cutoff of Dyer *et al* [13] to the 7.66 MeV reaction threshold indicates a 6.13 MeV γ-ray yield for E_α =8.8 MeV of 4×10^{-10} quanta per α. This yield contributes less than 1% to the 6–7 MeV bin in granite, and can be neglected in most calculations. Similarly for silicon, which has been shown by measurements at $E_\alpha = 10$ MeV [21] to produce no γ-rays above 6 MeV, and to have a yield approximately an order of magnitude less than aluminum below this energy, the published neutron yield is an order of magnitude below that of aluminum, and can be neglected in most calculations. This is supported by theoretical calculations [21], which indicate that Si reactions do not significantly contribute the γ-ray yield above $E_\gamma = 5$ MeV, and account for no more than 10% of the theoretical intensity distribution between 3 and 4 MeV in granite.

Carbon, although not present in granite, does occur in significant concentrations in some rocks. Available energy considerations indicate that the γ-rays from this element would primarily result from the (α,α') reaction on ^{12}C and the (α,n) reaction on the relatively rare ^{13}C isotope. The yield from the $^{13}\mathrm{C}(\alpha,n)$ reaction can be estimated in the same manner as that for oxygen, with the known neutron yield for carbon occurring at a rate approximately two orders of magnitude below that for Aℓ and Mg. Since carbon typically occurs in concentrations on the same order as that of Aℓ and Mg, the γ-ray contribution from this reaction is assumed to be at most on the 1% level in most materials and can be neglected in most calculations.

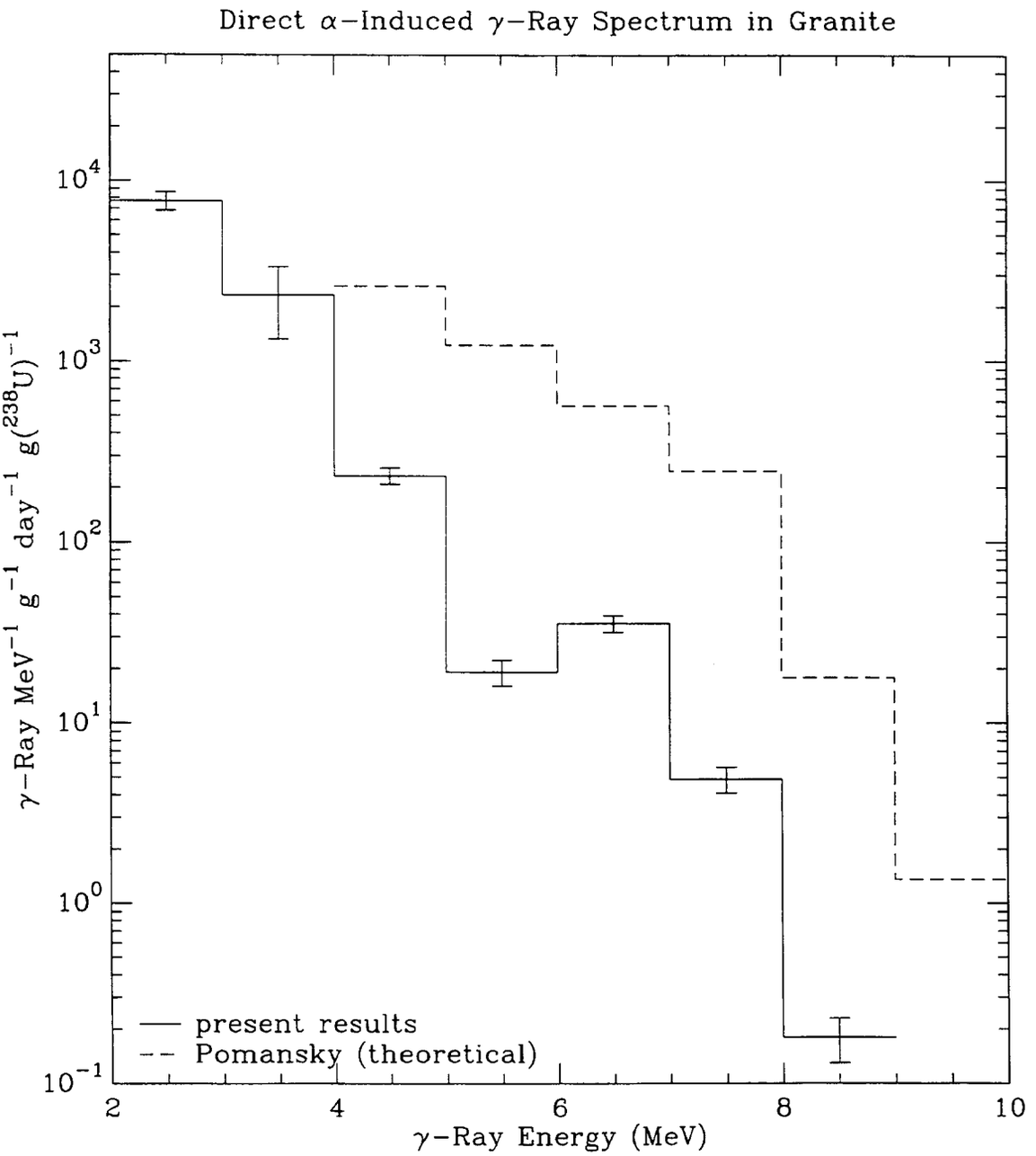

Fig. 6. The direct α-induced γ-ray spectrum in granite. The yields are reported in terms of the mass fraction of ^{238}U, with a concentration of ^{232}Th five times that of ^{238}U. The solid histogram shows the spectrum derived from experimental measurements. The broken-line histogram shows the theoretical calculations of Pomansky for granite with the same radioactive content.

The $^{12}C(\alpha,\alpha')$ reaction produces a significant γ-ray yield through the excitation of the first excited state at 4.439 MeV. A yield of 2.6×10^{-8} quanta per α and 2.3×10^{-6} quanta per α for 7.7 and 8.8 MeV α-particles, respectively, is obtained from an integration of the cross section measurements of Dyer *et al* [13]. The 8.8 MeV yield from this reaction is larger than the 4 to 5 MeV intensity distribution for the either Mg or Aℓ, and so should be incorporated into any calculation containing significant quantities of carbon. The 7.7 MeV yield is an order of magnitude smaller than that in Mg and Aℓ, and can be neglected in most calculations.

Although in many circumstances the direct-reaction component of the γ-ray spectrum from a material is a minor component of the total intrinsic γ-ray spectrum, under particular conditions, this background can become dominant. Such a situation occurs when the neutron induced background is highly suppressed in a material. A particular case where this occurs is in the Sudbury Neutrino Observatory (SNO).

The SNO detector is a large volume heavy water Čerenkov neutrino detector located in an ultra-low-background laboratory 2 km below ground level in the Creighton mine near Sudbury, Canada. The detector consists of 1000 tonnes of heavy water (D_2O) contained in a spherical acrylic vessel 12 m in diameter surrounded by a 7300 tonne light water shield. Neutrinos are detected from their reactions in D_2O and are observed through the Čerenkov light produced from the resulting relativistic electrons. An array of 9450 photomultiplier tubes fitted with aluminum light concentrators detects this characteristic signal. The photomultiplier tube array is arranged in an inward facing concentric geodesic shell, approximately 17 m in diameter and 2.5 m away from the acrylic vessel to provide a 60% surface area coverage of the D_2O [24,25].

The detector was carefully designed to minimize the high-energy γ-ray flux reaching the fiducial D_2O volume. The outer light water shield reduces the γ-ray flux from the granitic host rock, and at the same time moderates neutrons produced by trace radioactivity in the photomultiplier tube and aluminum light concentrators. These neutrons are largely captured by the boron component of the photomultiplier glass, and do not give rise to high energy γ-rays. In this case, the direct production component of the high energy γ-ray background becomes the dominant background source, accounting for 80% of the high energy γ-rays produced in the photomultiplier tube region of the SNO detector, which in turn account for 50% of the γ-rays reaching the fiducial volume [6].

The γ-ray spectra for the photomultiplier tube glass used in the SNO detector is presented in figure 7. Spectra from both the ^{238}U and ^{232}Th chains are shown in this figure for contamination levels of 1 ppm each. These spectra are dominated by γ-rays from α-particle reactions on boron.

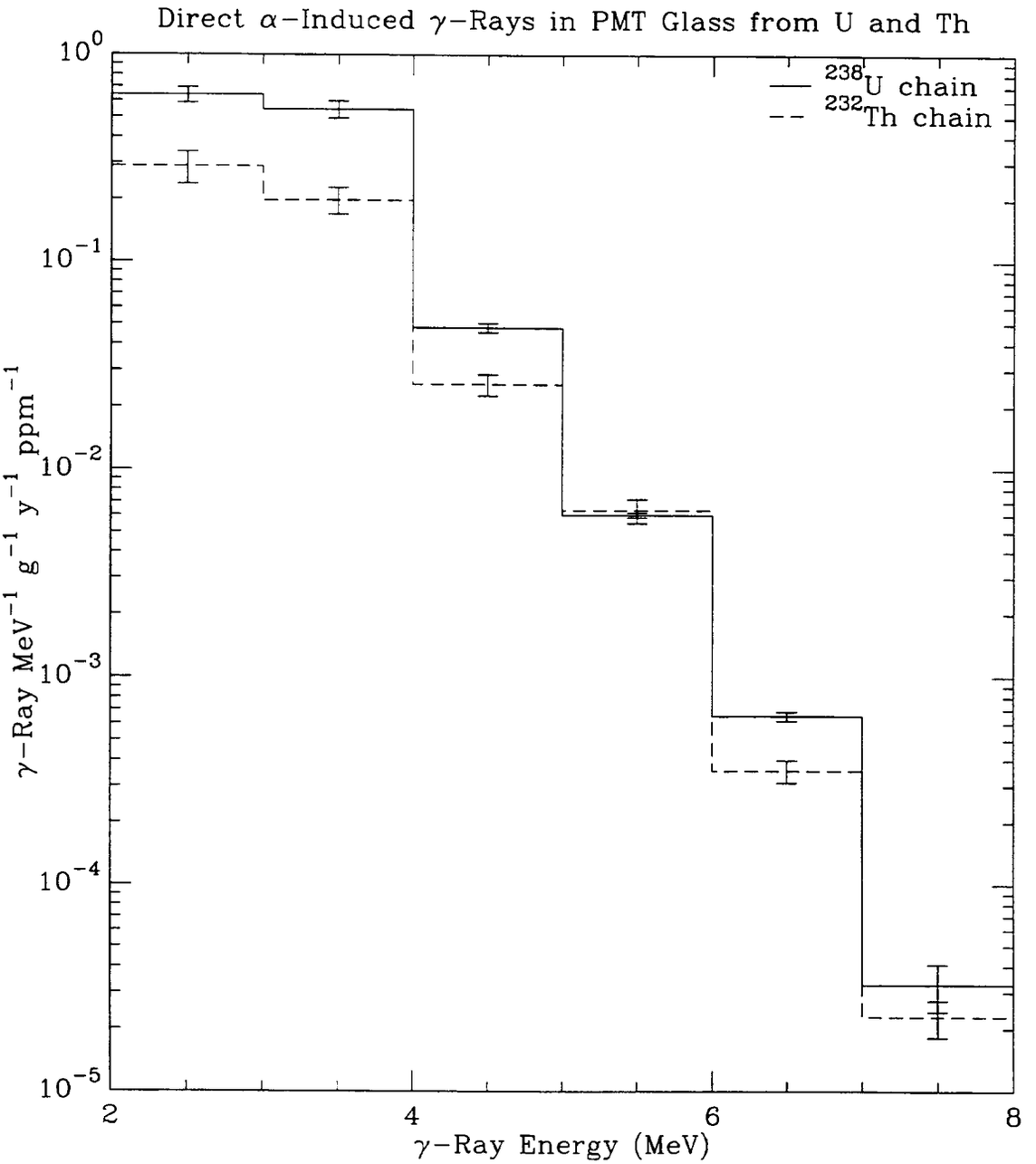

Fig. 7. The direct α-induced γ-ray intensity distribution in photomultiplier glass. The yields are reported for 1 ppm concentrations of both ^{238}U and ^{232}Th. The solid histogram shows the measurement-derived intensity distribution from ^{238}U, while the broken histogram shows the measurement-derived intensity distribution from ^{232}Th.

References

[1] Y. Feige, B. G. Oltman, and J. Kastner, *"Production rates of neutrons in soils due to natural radioactivity"*, Journal of Geophysical Research **73** (1968) 3135.

[2] D. West and A. C. Sherwood, *"Measurements of thick-target (α, n) yields from light elements"*, Annals of Nuclear Energy **9** (1982) 551.

[3] A. A. Pomansky, *"Underground low background laboratories of the Baksan Neutrino Observatory"*, Nuclear Instruments and Methods in Physics Research **B17** (1986) 406.

[4] R. Heaton, H. Lee, P. Skensved and B. C. Robertson, *"Neutron production from thick-target (α, n) reactions"*, Nuclear Instruments and Methods in Physics Research **A276** (1989) 529.

[5] R. Heaton, H. Lee, P. Skensved and B. C. Robertson, *"Alpha-induced neutron activity in materials"*, Nuclear Geophysics **4** (1990) 499.

[6] P. Skensved and B. C. Robertson, *"Summary of backgrounds in* SNO*"*, SNO Collaboration Report SNO-STR-94-13 (1994), unpublished.

[7] H. W. Sobel, A. A. Hruschka, W. R. Kropp, J. Lathrop, F. Reines, M. F. Crouch, B. S. Meyer and J. P. F. Sellschop, *"High energy gamma rays from spontaneous fission of ^{238}U"*, Physical Review C **7** (1973) 1564.

[8] A. G. Seamster, E. B. Norman, D. D. Leach, P. Dyer, and D. Bodansky, *"Cross sections relevant to gamma-ray astronomy: Alpha-particle-induced reactions"*, Physical Review C **29**, (1984) 394.

[9] K. W. Geiger and L. van der Zwan, *"Radioactive neutron source spectra from $^9Be(\alpha, n)$ cross section data"*, Nuclear Instruments and Methods **131** (1975) 315.

[10] K. W. Geiger and L. van der Zwan, *"An evaluation of the $^9Be(\alpha, n)$ cross section"*, National Research Council of Canada Report 15303, PXNR #2404 (1976).

[11] J. B. Seaborn, G. E. Mitchell, N. R. Fletcher, and R. H. Davis, *"Gamma rays from the $^9Be(\alpha, n_1)^{12}C$ reaction"*, Physical Review **129** (1963) 2217.

[12] V. V. Verbinski, F. G. Perey, J. K. Dickens, and W. R. Burrus, *"Neutrons from the $^9Be(\alpha, n)$ Reaction for E_α between 6 and 10 MeV"*, Physical Review **170** (1968) 916.

[13] P. Dyer, D. Bodansky, D. D. Leach, E. B. Norman, and A. G. Seamster, *"Cross sections relevant to gamma-ray astronomy: Alpha-particle-induced reactions on ^{12}C, ^{14}N, and ^{16}O nuclei"*, Physical Review **32** (1985) 1873.

[14] W. del Bianco, S. Kundu, and J. Kim, *"The $^{11}B(\alpha, \gamma_0)^{15}N$ reaction in the giant dipole resonance region"*, Canadian Journal of Physics **55** (1977) 302.

[15] A. Degré, M. Schaeffer, G. Bonneaud and I. Linck, *"Experimental study of the radiative capture* $^{11}B(\alpha,\gamma_0)^{15}N$ *for* $15.5 \leq E_x \leq 19.5$ *MeV"*, Nuclear Physics **A306** (1978) 77.

[16] R. K. Heaton, H. W. Lee, K. T. Lesko, E. B. Norman, B. Sur, and B. C. Robertson, *"α-Particle induced γ-ray transitions in light elements"*, in preparation.

[17] F. Ajzenberg-Selove, *"Energy levels of light nuclei A = 18–20"*, Nuclear Physics **A475** (1987) 1.

[18] P. M. Endt *"Energy Levels of A = 21–44 Nuclei (VI)"*, Nuclear Physics **A310** (1978) 1.

[19] P. M. Endt *"Energy Levels of A = 21–44 Nuclei (VII)"*, Nuclear Physics **A521** (1990) 1.

[20] J. F. Ziegler, J. P. Biersack, U. Littmack, *"The Stopping and Range of Ions in Solids"* in **The Stopping and Ranges of Ions in Matter**, Pergamon Press: New York (1985).

[21] R. Heaton, *"The α-Induced Thick-Target γ-Ray Yield from Light Elements"*, Ph.D. Dissertation, Queen's University (1994).

[22] V. I. Glotov, *"γ-Radiation from the earth and neutrino experiments"*, translated from Atomnaya Énergiya **30** (1971) 384.

[23] V. I. Glotov, *"Radiation background of the external environment and methods of reduction for solar neutrino experiments"* Ph.D. Dissertation (in Russian), Soviet Academy of Sciences, Institute of Nuclear Research, USSR, (1978), unpublished.

[24] C. E. Waltham, E. D. Hallman, P. Doe, R. G. H. Robertson, W. Frati, R. Van Berg, K. T. Lesko, B. C. Robertson, J. J. Simpson, *"Research and development for the Sudbury Neutrino Observatory"*, Physics in Canada **48** (March 1992) 135.

[25] B. C. Robertson, SNO*: A multifunction spectrometer for solar neutrinos"*, in **Perspectives in Neutrinos, Atomic Physics and Gravitation**, J. Trân Thanh Vân, T. Damour, E. Hinds and J. Wilkerson (eds.), XIII Moriond Workshop: Editions Frontieres (1993) 119.